Oxide at the Al-rich Fe$_{0.85}$Al$_{0.15}$(110) surface

Zongbei Dai,[1] Natalia Alyabyeva [ORCID],[1] Maxime Van den Bossche,[1] Patrizia Borghetti,[1] Stéphane Chenot,[1] Pascal David [ORCID],[1]
Alexey Koltsov [ORCID],[2] Gilles Renaud,[3] Jacques Jupille,[1] Gregory Cabailh [ORCID],[1] Claudine Noguera [ORCID],[1]
Jacek Goniakowski [ORCID],[1] and Rémi Lazzari [ORCID][1,*]

[1]*CNRS, Sorbonne Université, Institut des NanoSciences de Paris, UMR 7588, 4 Place Jussieu, F-75005 Paris, France*
[2]*ArcelorMittal Maizières Research, voie Romaine, F-57280, Maizières-lès-Metz, France*
[3]*Université Grenoble Alpes, CEA, INAC, MEM, 38000 Grenoble, France*

The formation of an ultrathin aluminum oxide film at the Fe$_{0.85}$Al$_{0.15}$(110) surface (A$_2$ random alloy) has been studied by a variety of surface-sensitive techniques (x-ray photoemission, low-energy electron diffraction, surface x-ray diffraction, and scanning tunneling microscopy) supplemented by *ab initio* atomistic simulations. Since iron is not oxidized in the conditions used, the study focused on the coupling between aluminum oxidation and segregation processes. Compared to the bare surface, whose average composition (Fe$_{0.6}$Al$_{0.4}$) is closer to the B$_2$-CsCl structure over a $\sim$3 nm depth, the oxidation hardly affects the subsurface segregation of aluminum. All the structural and chemical fingerprints point to an oxide film similar to that found on NiAl(110). It is a bilayer ($\sim$7.5 Å thick) with a composition close to Al$_{10}$O$_{13}$ and a large (18.8 $\times$ 10.7) Å^2 nearly rectangular unit cell; an almost perfect match between substrate periodicity and the (1 $\times$ 2) oxide supercell is found. Nevertheless, microscopy reveals the presence of antiphase domain boundaries. Measured Al 2p and O 1s core-level shifts match calculated ones; their origin and the relative contributions of initial/final state effects are discussed. The ubiquity of the present oxide on different supports asks for the origin of its stability.

I. INTRODUCTION

In binary A$_{1-x}$B$_x$ alloys, in which the B species has a higher oxygen affinity than A, internal or external oxidation [1,2] in the form of a BO$_y$ compound may occur, depending on oxygen activity. Prototypical examples are chromia on *M*-Cr alloys (M = Fe [3], Co [4,5], Ni [6,7]), and alumina on Al-alloyed bimetallic single crystal surfaces (FeAl [8–12], CuAl [13–15] and CoAl [16,17]) with a focus on NiAl surfaces [18–24], especially NiAl(110) [25–31]. Studied *per se* for high-temperature applications [32], the alumina films [2] of limited thickness (5–11 Å [25,33,34]) formed on NiAl [26,35,36] and Ni$_3$Al [37,38] low-index surfaces (Ni is never oxidized) were used mainly as catalyst supports [2,39,40]. The oxide structure on NiAl(110) was first described as close to α-, γ-, and κ alumina [18,25,41,42]. A combination of scanning tunneling microscopy (STM) and *ab initio* calculations then concluded to a bilayer oxide film, whose large quasirectangular unit cell is nearly commensurate along its diagonal, with a 4(Al$_4^{2+}$O$_6^{2-}$Al$_6^{3+}$O$_7^{2-}$) stacking sequence involving interfacial (Al$_i$ and O$_i$) and surface (Al$_s$ and O$_s$) Al and O ions [29] (Fig. S1, Supplemental Material [43]). This structure without a bulk counterpart matches perfectly diffraction [18], near-field microscopy [29,44–47], and spectroscopic data [25,29,31].

The oxidation of FeAl alloys received much less attention [9], despite many practical applications. The oxidation at 773–1173 K of B$_2$-Fe$_{0.47}$Al$_{0.53}$(110) leads to well-ordered

6 $\pm$ 1 Å thick oxide films covering the whole surface [9], whose structure was suggested to involve a quasirectangular unit cell with two domains, as on the oxidized NiAl(110) surface. Besides this structure, a streaked phase was observed upon oxidation above 773 K, indicating long-range order (disorder) along the [001] ([1$\bar{1}$0]) direction. (Notably, similar streaks observed on the bare Fe$_{0.85}$Al$_{0.15}$(110) were assigned to carbon contamination [48].) Quite differently, the existence of an oxide unit cell (18.6 $\times$ 19.4) Å^2 rotated by 30$°$ relative to the [1$\bar{1}$0] direction was postulated on oxidized FeAl(110) [10,11], in line with a theoretical model [49,50]. Finally, an x-ray diffraction study [51] of clean Fe$_{0.75}$Al$_{0.25}$(110) revealed a B$_2$ surface layer on a bulk D0$_3$ order; upon oxidation at 573 K, a surface oxide is formed while the order disappears within a 2–3 nm thick Al-depleted subsurface region. In the blurred landscape of FeAl oxidation, applications prompted us to focus on the (110) surface of the random Fe$_{0.85}$Al$_{0.15}$ alloy. The oxygen-induced formation of alumina at the surface of Al-alloyed advanced high strength steel used by the automotive industry to lower car weight and fuel consumption [52,53] is an issue for the wetting and stability of the anticorrosive zinc coating. The Al-alloyed steel study being out of grasp, Fe$_{0.85}$Al$_{0.15}$ offers a relevant model system which crystallizes up to its melting point (1700 K) in an A$_2$ body-centered cubic ferrite phase similar to that found in Al-alloyed steel. The dense (110) orientation was chosen because it shows a defined surface structure [54,55].

Unlike bulk-terminated ordered intermetallic compounds such as D0$_3$ (Ni$_3$Al) or B$_2$ (NiAl, FeAl), the bare Fe$_{0.85}$Al$_{0.15}$(110) surface tends to be enriched in aluminum which segregates above 700 K over a $\sim$3 nm thick region

*Corresponding author: remi.lazzari@insp.jussieu.fr

with an average composition of $Fe_{0.6}Al_{0.4}$ [54,55]. Therefore, the question at hand, poorly tackled in surface science, is the coupling between Al oxidation and segregation. Following herein a logical order, the topography of the oxide film is studied first by STM. Then, oxide composition and thickness are determined by x-ray photoemission spectroscopy (XPS) while the structure is analyzed by low-energy electron diffraction (LEED) and grazing-incidence x-ray diffraction (GIXD). Finally, the consistency of the approach is discussed via *ab initio* calculations of core-level shifts (CLSs).

II. METHODS

A. Experimental

Experiments were conducted at INSP in two connected preparation and analysis ultrahigh vacuum (UHV) chambers, with base pressures of $1.5 \, 10^{-10}$ mbar and $<1.0 \, 10^{-10}$ mbar, respectively. Surface composition and segregation profile [48,54,55] were analyzed by XPS under Al-Kα monochromatic excitation (1486.6 eV; Phoibos 100 hemispherical analyzer from SPECS) at a pass energy of 20 eV for angles ranging from normal ($\Theta = 0°$) to grazing emission ($\Theta = 75°$). Structures were determined by LEED, as well as GIXD performed on the UHV chamber of the BM32 beamline at the European Synchrotron Radiation Facility [55]. STM (RT-Omicron) was run at room temperature with a KOH (potassium hydroxide) electrochemically etched W tip. Images were processed using WSxM [56] software for background subtraction and profile analysis.

The same $Fe_{0.85}Al_{0.15}(110)$ single crystal (diameter 6 mm; thickness 2 mm; miscut below $0.1°$) was used for all measurements. It was cleaned in UHV via cycles of Ar^+ sputtering (1 keV; 30 min) followed by annealing at 1193 K in UHV (during $\sim$15 min at a few 10^{-9} mbar) [48,54,55], a temperature at which the Al segregation profile reaches a plateau value according to XPS [54]. Heating and cooling rates were around 250 K/min. Oxide films were synthesized in a single step at 1073–1123 K (right after cooling down from the last substrate annealing at 1193 K) under an O_2 partial pressure of $10^{-7} - 10^{-6}$ mbar. As on NiAl(110) [30,33], a two-step oxidation via room temperature O_2 exposure and annealing gives similar LEED fingerprints (not shown). At higher temperature (1193 K), the surface does not oxidize, meaning that O_2 does not stick; however, the oxide formed at 1073–1123 K withstands an annealing up to 1273 K without decomposition. The oxide was judged by LEED and STM to completely cover (see below) the surface above 50 L O_2 (one Langmuir is defined as $1.33 \, 10^{-6}$ mbar/s) with no change or thickening up to 500 L. In what follows, oxidized surface refers to an initially bare clean $Fe_{0.85}Al_{0.15}(110)$ surface annealed at 1193 K with a fully developed Al segregation that is exposed at 1073–1123 K to more than 50 L of O_2, all preparations being performed *in situ* in UHV conditions.

The superstructure matrix M_S of the oxide unit cell is described herein using the $(\mathbf{a}_S, \mathbf{b}_S)$ rectangular centered surface unit cell (index S) of $Fe_{0.85}Al_{0.15}(110)$ bulk truncation (index B) along the $[1\bar{1}0]_B$ and $[001]_B$ bulk directions. Its parameters are $a_S = 4.0891 \, \text{Å}$ and $b_S = 2.8914 \, \text{Å}$ (bulk lattice parameter $a_B = 2.8914 \, \text{Å}$ [57]). Diffraction indexes (h_S, k_S, l_S) are

defined in the corresponding reciprocal unit cell, l_S direction being normal to the $(110)_B$ plane.

B. Simulations

The present experimental work was supplemented by density-functional theory (DFT) [58,59] calculations using the plane wave projector augmented-wave [60] (PAW) code VASP [61–64]. Exchange-correlation effects were treated with optB86b-vdW [65,66]. This functional combines (i) semilocal exchange with a modified B86b expression [67], (ii) correlation in the local density approximation [59], and (iii) long-range van der Waals correlation using the vdW method [68,69]. The basis set included plane waves up to a kinetic energy of 500 eV. Considering the large size of the parallelogram-shaped $\begin{bmatrix} 5 & 1 \\ 2 & 7 \end{bmatrix}$ oxide surface unit cell employed here as in Ref. [29] on NiAl(110) (Fig. S1 [43]), restricting the Brillouin-zone sampling to the Γ point was sufficient. As explained in Sec. VI, simulations were performed on the ordered B2-CsCl FeAl(110) surface. Standard PAW setups were used for all elements with valences of 3, 6, and 8 for Al, O, and Fe, respectively. The use of spin polarization was considered but the influence on the properties of interest was found to be very limited. Geometry optimization was carried out with four-layer metal slabs (with the bottom two layers fixed to their bulk positions) and pursued until the forces are less than $5 \cdot 10^{-2}$ eV/Å in magnitude. After relaxation, three more metal layers were added at the bottom of the slab to ensure sufficiently bulklike references in the middle layer.

The CLSs were calculated in the well-validated [70,71] complete screening approach, which includes the response of the valence electrons to the creation of a core hole. Screening by other core electrons were not taken into account in the present implementation, as it is generally environment independent and therefore does not significantly influence the CLS [70]. To analyze the origin of the calculated shifts, these were furthermore decomposed into initial and final state contributions. The former is defined as the negative of the corresponding difference in Kohn-Sham eigenvalues of the core levels in the unperturbed structure, which are closely related to differences in the electrostatic potential in the vicinity of the atomic cores. The latter contribution represents differences in energy transferred to the photoelectron by valence electrons which screen the newly formed core hole.

III. OXIDE TOPOGRAPHY FROM STM

On large scale STM images, the oxidized $Fe_{0.85}Al_{0.15}(110)$ surface (Fig. 1) appears as homogeneously covered by a continuous oxide layer. The pseudohexagonal reconstruction of the bare surface (18 Å period) [55] is completely lifted. The stability of the oxide film after an overnight aging in STM (not shown) proves a chemical inertness that allows for long-term analyses. Unlike on the bare surface [55], step bunching is observed with large 25–500 nm terraces separated by steps from 2 to 40 Å high [Fig. 1(a)]. Spaced stripes preferentially aligned close to the $[001]_B$ direction appear on terraces [Fig. 1(b)]. They are separated by 8–12 nm, as confirmed by line profile and Fourier analysis [Fig. 1(c)]. Between stripes, a higher resolution [Fig. 2(c)] evidences a
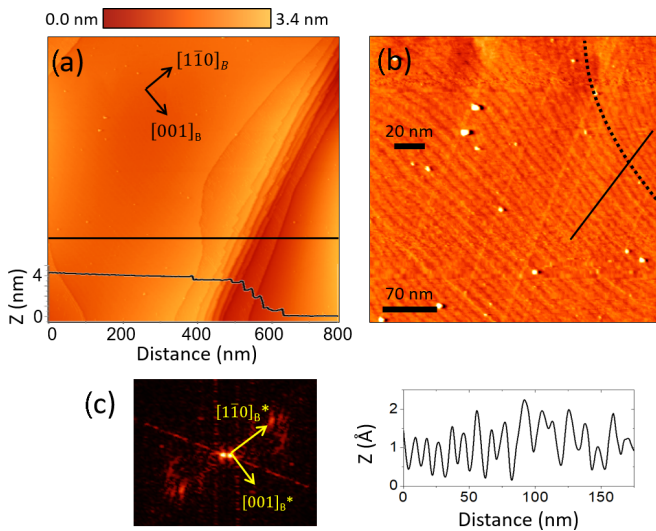
FIG. 1. STM images ($U_b = 1$ V, $I_t = 100$ pA) of the oxidized $Fe_{0.85}Al_{0.15}(110)$ surface: (a) (800×800) nm^2 image and profile (in inset) along the continuous line; (b) (350×350) nm^2 image of a terrace evidencing the stripe domains; (c) corresponding Fourier analysis and topography profile along the continuous line of (b).

~ 2 nm periodic structure tilted from the $[1\bar{1}0]_B$ direction. The domains are limited by ~ 3-nm-wide boundaries in which the periodic motif is shifted by a fraction of a period with anti-correlated amplitudes as seen in topography profiles (Fig. 2; green/black lines). This observation rules out a moiré effect.
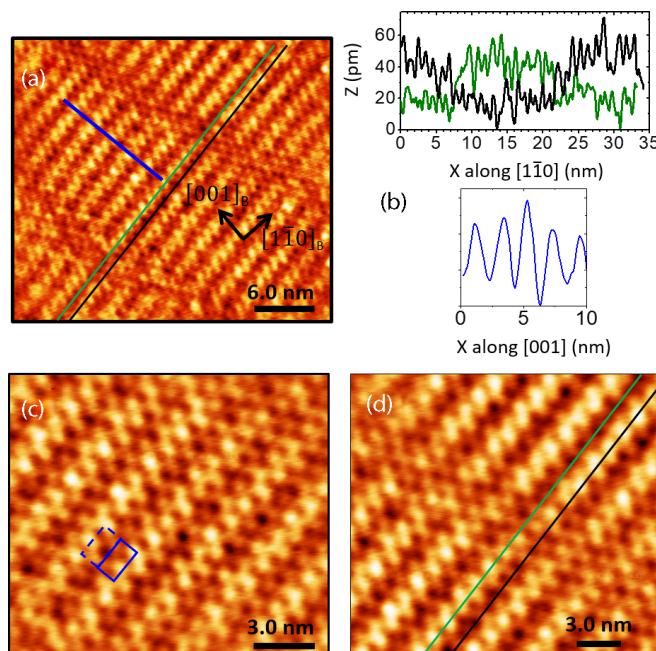

FIG. 2. High-resolution STM images ($U_b = -1$ V, $I_t = 12$ pA) of the oxidized $Fe_{0.85}Al_{0.15}(110)$ surface: (a) (30×30) nm^2 of stripe domains and boundaries between them; (b) topography profiles along green, black, and blue lines in (a); (15×15) nm^2 image of the oxide reconstruction (c) in the center and (d) at boundary of the domains. The (1×2) coincidence of the (18.8×10.6) Å^2 oxide unit cell determined by diffraction is shown in blue in (c).

Despite distortions related to small domain size, the imaged "periodic" structure matches the oxide unit cell determined by diffraction in Sec. V [Fig. 2(c)].

Such a topography is very similar to that of the oxidized NiAl(110) [18,26,45,46,72–76] where antiphase domain boundaries have been observed and assigned to misfit dislocations [73,74] accompanied by an oxygen deficient line of atoms [46,74]. As in the present case, these defects appear in the form of a shift of periodicity between domains [26,72–74,77]. But in contrast to NiAl(110) where they appear as irregular shaped lines, reflection domain boundaries due to the twofold symmetry of the substrate (see diffraction analysis in Sec. V) are not clearly evidenced on large terraces. They are rather revealed by progressive rotations of the antiphase domain boundaries [see dotted line in Fig. 1(b)].

In conclusion, the STM study demonstrates the crystallographic quality of the film, its continuity, and its stability against aging, that are all important results to ensure the validity of the experimental analysis.

IV. PHOTOEMISSION ANALYSIS

A. Core-level line shapes

On the oxidized $Fe_{0.85}Al_{0.15}(110)$ surface, the perfect overlap of Fe 3p before and after oxidation even at grazing emission [Fig. 3(a)] proves that Fe remains metallic since a positive binding energy (E_B) shift is expected for oxidized Fe ($E_B = 52.9 \pm 0.3$ eV for Fe; 55 ± 0.6 eV for FeO; 55.1 ± 1 eV for Fe_3O_4; 55.9 ± 0.4 eV for Fe_2O_3; 56.2 ± 1 eV for FeOHO) [78–80]. Conversely, the enhancement at grazing emission of an Al 2p shoulder shifted relative to the metal ($E_B = 72.1$ eV) points to the formation of an aluminum oxide film [Fig. 3(b)] in accordance with the difference in electronegativity between the two elements ($I_{Fe} = 1.83$; $I_{Al} = 1.61$; Pauling's scale [81]). As suggested by a simple visual inspection of Fig. 3(b) and in a similar way as on NiAl(110) [31], the Al 2p spectra is decomposed into three components made of doublets with a spin orbit splitting of 0.4 eV [80] and a theoretical value of $1/2$ of the $2p_{1/2}/2p_{3/2}$ branching ratio (Table I). A Shirley background [82] was subtracted during fits. Metallic and oxide components were accounted for by Doniach-Sunjic (DS) [83] and Voigt (V) profiles, respectively. A similar DS asymmetry of 0.1 was found for metallic Al on bare and oxidized surfaces. The Lorentzian broadening was kept close to the Al K-α emission width (0.58 eV) [78]. The instrumental and sample-related broadening due to binding energy distribution was introduced through the Gaussian part of the Voigt function. In a similar way, the O 1s profile was decomposed into two Voigt components (Table II).

The clean FeAl(110) surface is of pure metallic character, as evidenced by the unique DS profile of Al 2p [Fig. 3(b) and Table I]. Moreover, the difference between the observed E_B (72.1 eV) and the tabulated value (72.6 $\pm$ 0.3 eV) [80] is characteristic of Fe-Al binding in aluminides [84]. On the oxidized surface, the comparison to E_B values found for Al_2O_3 (74.1 $\pm$ 1 eV) [80] or oxidized Al (74.4 $\pm$ 1.5 eV) [80] favors the occurrence of Al^{3+}. Changes in relative intensity observed from normal to grazing emission [Fig. 3(b) and Table I] allows the assignment of the higher (lower) shifted
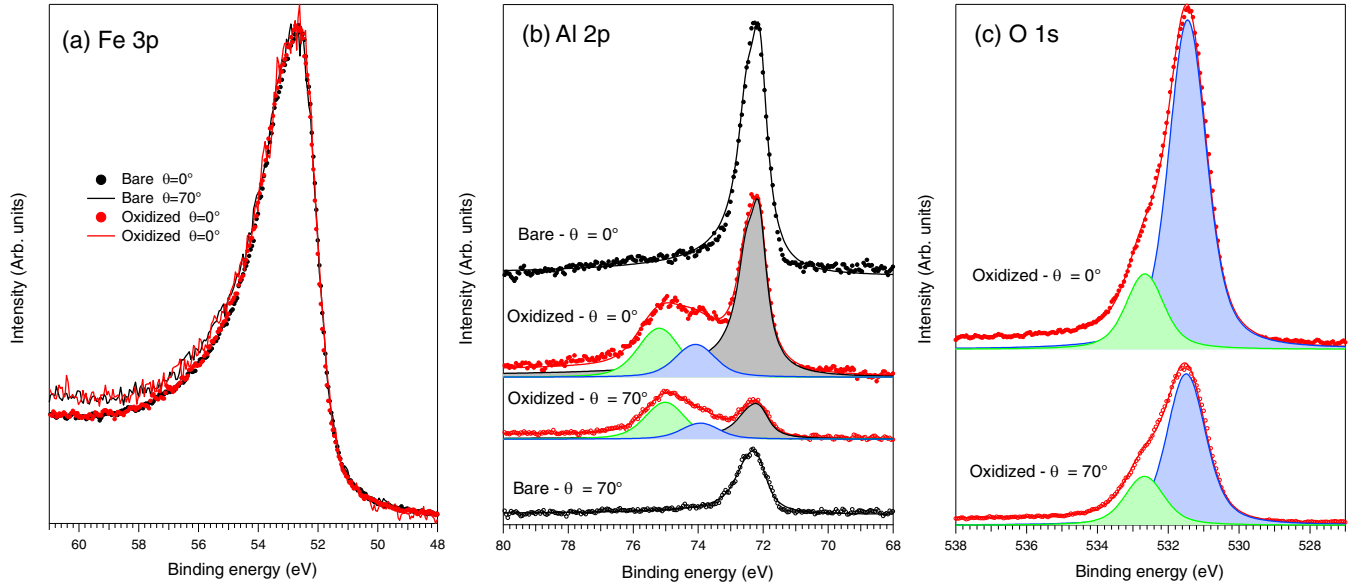
FIG. 3. Comparison at normal ($\Theta = 0°$) and grazing ($\Theta = 70°$) emissions of the core-level spectra recorded on the bare (1193 K) and oxidized $Fe_{0.85}Al_{0.15}(110)$ surface: (a) Fe $3p$, (b) Al $2p$, and (c) O $1s$. Points correspond to data and continuous lines to fits (see text); fit parameters are given in Tables I and II.

Al $2p$ component to surface (interface) Al atoms (Fig. S2(b) [43]). Parallel assignments can be made for the O $1s$ spectrum, as the intensity of the component of higher E_B (surface) is enhanced at grazing emission [Fig. 3(c) and Table II]. A quantitative comparison to DFT results and to the NiAl(110) case both in terms of binding energies and relative area will be presented in Sec. VI.

B. Similarity of the Al segregated profile on bare and oxidized surfaces

The larger Gaussian broadening of the metallic Al core level at grazing emission indicates a distribution of E_B due to segregation [48,54,55]. Keeping fixed the above core-level decomposition, the Al concentration profile underneath the oxide was derived from the variation with emission angle

TABLE I. Parameters of the Al $2p$ core-level decomposition [Fig. 3(b)]. Binding energy (E_B) and Gaussian full width at half maximum (G-FWHM) for bare (1193 K) and oxidized surfaces are compared at either normal ($\Theta = 0°$) or grazing emissions ($\Theta = 70°$). The symbols DS, V, M, S, and I stand for Doniach-Sunjic, Voigt, metal, surface, and interface, respectively. Error bars are ~10% for areas and ~0.05 eV for energies.

	Angle	Shape	Type	Rel. area	E_B (eV)	G-FWHM (eV)
Clean	$\Theta = 0°$	DS	M	1.0	72.10	0.10
Clean	$\Theta = 70°$	DS	M	1.0	72.20	0.35
Oxide	$\Theta = 0°$	DS	M	0.66	72.10	0.10
		V	I	0.13	74.00	1.00
		V	S	0.21	75.1	1.10
Oxide	$\Theta = 70°$	DS	M	0.40	72.10	0.33
		V	I	0.175	73.80	0.90
		V	S	0.425	74.9	1.00

of the $I^c_{Al\,2p}/I^c_{Fe\,3p}$ area ratio of metallic components (Fig. S2 [43]) corrected for photoionization cross sections and analyzer transmission functions [48,54,55] (with the advantage that the neighboring Al $2p$ and Fe $3p$ E_B lead to the same escape depth). A profile similar as on the bare surface [54] is found (Fig. 4). To quantify it, the angular variation was fitted [54] by assuming either (i) a homogeneous segregated layer $Fe_{1-x_S}Al_{x_S}$ of thickness t_S on top of a $Fe_{0.85}Al_{0.15}$ bulk composition or (ii) a continuous diffusive profile $Fe_{1-x_S(z)}Al_{x_S(z)}$ with a depth(z)-dependent surface composition $x_S(z) = x_B + \Delta x \exp(-z^2/\Lambda^2)$, where Λ is a segregation characteristic length [54]. As on the bare surface [54], the two models fit equally well the data (not shown). The bare surface profile characteristics [$x_S(z = 0) = x_B + \Delta x = 0.40 \pm 0.03$, $t_S = 30 \pm 7$ Å, $\Lambda = 36 \pm 10$ Å] do not evolve upon oxidation [$x_S(z = 0) = 0.41 \pm 0.03$, $t_S = 27 \pm 6$ Å, $\Lambda = 32 \pm 8$ Å]. Bulk diffusion of Al should compensate for the oxide formation since the Al contribution to the oxide layer [~0.2 Al atom/Å^2 for an oxide structure similar to that found on NiAl(110)] is a significant fraction in comparison to that of the segregated layer (~1 Al atom/Å^2).

According to the bulk phase diagram [85–88], the average composition underneath the oxide corresponds to the ordered CsCl-type B_2 phase, as on the bare surface [54].

TABLE II. Fit results for the O $1s$ core level of the oxide film. Parameters and symbols have the same meaning as in Table I.

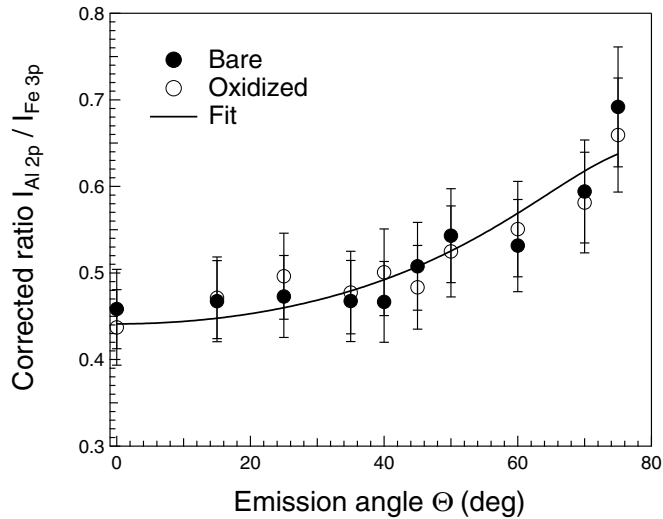| Angle	Shape	Type	Rel. area	E_B (eV)	G-FWHM (eV)
$\Theta = 0°$	V	S+I	0.81	531.45	0.90
	V	S	0.19	532.65	0.90
$\Theta = 70°$	V	S+I	0.76	531.50	1.00
	V	S	0.24	532.65	1.00

FIG. 4. Comparison of angular variation of the corrected ratio $I^c_{(Al\,2p\text{metal})}/I^c_{Fe\,3p}$ for the metallic components on the bare (filled circles) and oxidized (open circles) $Fe_{0.85}Al_{0.15}(110)$ surface. The chosen error bars of 10% on the experimental ratio match with data dispersion. The continuous line corresponds to a fit with a continuous segregation profile (see text).

FIG. 5. Model-dependent thickness of the oxide layer as derived from various photoemission intensity ratios (see text). (i) Model 1 (dotted lines): Al_2O_3 film on the $Fe_{0.85}Al_{0.15}$ bulk. (ii) Model 2 (full lines): Al_2O_3 film on the segregation profile found in Sec. IV B. (iii) Model 3 (dots): $Al_2O_{2.5}$ film on the same segregation profile.

C. The stoichiometry and thickness of the oxide film

From oxide and substrate core-level area ratios $I^c_{Al2p(\text{oxide})}/I^c_{Fe3p}$, $I^c_{Al(\text{oxide})}/I^c_{Al(\text{metal})}$, I^c_{O1s}/I^c_{Fe3p}, $I^c_{O1s}/I^c_{Al2p(\text{metal})}$, photoemission is now used to determine the composition and thickness of the continuous oxide layer observed by STM (Sec. III). The respective roles of the Al concentration gradient and the oxide composition in the modeling are highlighted by three approaches of increasing sophistication (see Sec. SII [43] for details). The first model (the simplest representation) ignores segregation and pictures an Al_2O_3 layer on a homogeneous $Fe_{0.85}Al_{0.15}$ bulk. It leads to a huge discrepancy between the signals normalized to metallic Al $2p$ and Fe $3p$ components, with a factor of three between the estimates of the oxide thickness (model 1; dotted lines in Fig. 5). A second model (Sec. SII [43]) involves the previously determined subsurface continuous segregation profile; the Al_2O_3 thickness was calculated from Eqs. (S1) and (S2) [43] with a 10% standard deviation (Fig. 5). Consistent fits are obtained (model 2; full lines in Fig. 5) with, however, a flaw. The curves normalized with respect to either Al $2p$ or Fe $3p$ overlap nicely, but do not agree with each other, which suggests that a problem comes not from the segregation profile but from the oxide itself. This likely is an understoichiometry in oxygen relative to Al_2O_3 since a lower film thickness is obtained when O $1s$ is taken as reference. Indeed, an oxide composition $Al_2O_{2.5\pm0.2}$ close to that found on NiAl(110) i.e., $Al_{10}O_{13} = Al_2O_{2.6}$ [18,29,89] leads to fair agreement (model 3; dots in Fig. 5). The film thickness of 7.5 Å is consistent with a bilayer as on NiAl(110). The robustness of the determined values with respect to emission angle validates the hypothesis of film continuity. The chemical analogy with the oxide structure found on NiAl(110) is further discussed below on the basis of
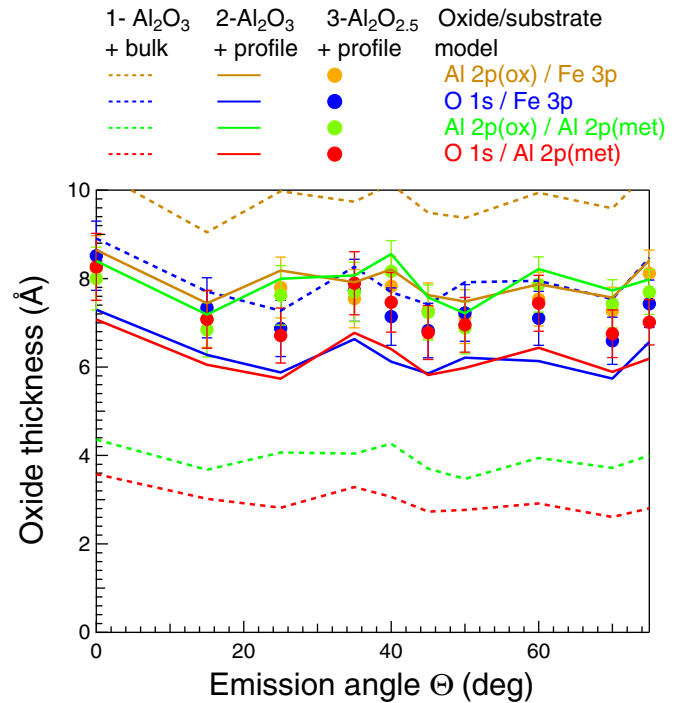
ab initio calculations of CLSs (Sec. VI). But a prerequisite is the determination of the oxide layer unit cell.

V. THE OXIDE UNIT CELL FROM DIFFRACTION

The LEED pattern of the oxidized $Fe_{0.85}Al_{0.15}(110)$ is shown in Figs. 6(a) and 6(b). The $\{11\}_S$ substrate reflections remain visible [Fig. 6(b)] but the flowerlike fingerprints of the bare surface reconstruction [54] are not anymore. The two mirror planes crossing at the center of the reciprocal space are compatible with a *pmm*, a subgroup of the *cmm* rectangular centered surface unit cell. The pattern shows similarities with those obtained on oxidized NiAl(110) [26] and FeAl(110) [9]. They can be indexed with a rotated quasirectangular unit cell [Fig. 6(d)] which, due to the *cmm* symmetry, gives rise to two domains. A comparison [90] (not shown) with the superstructure matrix $M_S = \begin{bmatrix} 4 & 2.53 \\ -1 & 3.37 \end{bmatrix}$ proposed for the oxidized FeAl(110) [9] by analogy to that obtained on NiAl(110) [26] led to a poor agreement with the main central spots pointing at a slightly distorted mesh. The limits of the LEED analysis (distortions due to sample position and tilt) led us to perform a quantitative analysis by GIXD.

Figure 7 compares in-plane reciprocal scans along the $[10]_S$ and $[01]_S$ directions before (bare surface) and after oxidation. Radial scans overlap along the $[01]_S$ direction. In parallel, the superstructure peaks [54] along $[10]_S$ at $h_S = (1.56 - 3.56 - 5.56, 0, 0.075)$ are lifted by oxidation. This demonstrates that, while the formation of the continuous oxide layer does not change the profile of segregation underneath
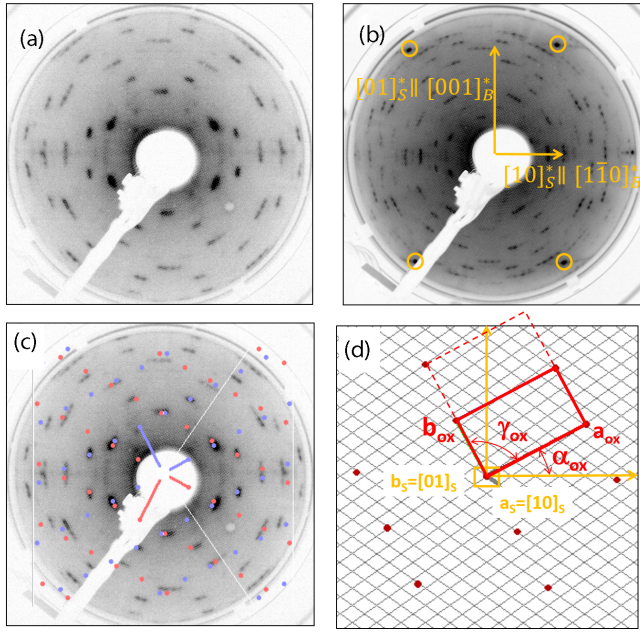
FIG. 6. Surface structure of the oxidized $Fe_{0.85}Al_{0.15}(110)$ surface (exposure 50 L): LEED patterns at a beam energy of (a) 45 eV and (b) 109 eV; in (b), the substrate $\{11\}_S$ reflections are circled in orange and the reciprocal substrate directions $[10]_S^* \parallel [1\bar{1}0]_B^*$ and $[01]_S^* \parallel [001]_B^*$ (S and B indexes stand for surface and bulk, respectively) are shown. (c) Comparison between LEED pattern of (b) and that obtained by a simulation using the superstructure matrix derived from GIXD. Red and blue dots correspond to the two mirror-symmetry-related domains. (d) Corresponding real space of one of the two oxide domains. The centered substrate rectangular unit cell ($\mathbf{a}_S = [10]_S$, $\mathbf{b}_S = [01]_S$) is in orange. The grey grid corresponds to the substrate primitive unit cell. The drawing highlights the (1×2) coincidence of the oxide unit cell ($\mathbf{a}_{ox}, \mathbf{b}_{ox}$) on the substrate (see grey grid). γ_{ox} is the angle between the oxide unit cell vectors ($\mathbf{a}_{ox}, \mathbf{b}_{ox}$) and α_{ox} is the angle between $\mathbf{a}_{ox}$ and $\mathbf{a}_S$.

FIG. 7. Comparison of GIXD in-plane radial scans ($l_S = 0.0075$) performed on the bare (black line) and oxidized (blue line) $Fe_{0.85}Al_{0.15}(110)$ surfaces: (a) (h_S, 0, 0.075) and (b) (0, k_S, 0.075). Vertical grey (blue) lines point at peaks due to the clean surface reconstruction (oxide-related features). Curves have been shifted for clarity.

(Sec. IV B), it impacts the nature of the pseudohexagonal surface superstructure [55] of the segregated layer by releasing the "incommensurate" direction. Of course, new peaks characteristic of the oxide layer itself appear in Fig. 7 (blue lines).

To isolate the oxide-related diffraction features, limited portions of the in-plane reciprocal space (at $l_S = 0.075$) of the bare (Fig. S4 [43]) and oxidized (Fig. 8) surfaces were mapped with GIXD through angular ω scans. Obvious powderlike spurious spots due to crystal imperfections and reflections from the substrate structure are excluded from the analysis (grey open squares in Fig. 8). Within a set of identified potential oxide reflections (green circles), three aligned intense spots (noncolinear with the substrate directions) are undoubtedly in-plane Bragg reflection of the same oxide domain (large black circles in Fig. 8 and reflections 1,2,3 in Table SII [43]). From these three spots, the most likely oxide unit-cell parameters ($a_{ox}, b_{ox}, \gamma_{ox}, \alpha_{ox}$) [see Fig. 6(d) for definitions of angles γ_{ox}, α_{ox}] and reflection indexing [(h_{ox}^i, k_{ox}^i), $i = 1 \ldots 3$] were sought in a way which is detailed in Sec. SIII [43]. The principle of the analysis is to use the theoretical link between (h_{ox}^i, k_{ox}^i) and (h_S^i, k_S^i) (Eqs. (S3) and (S4) [43]) to define
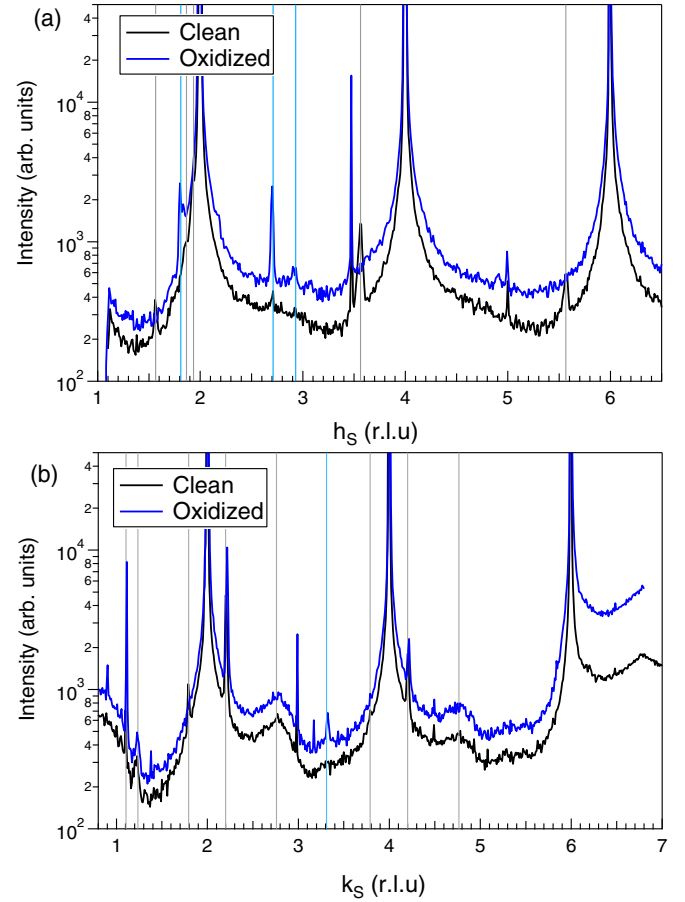
a cost function χ^2 on the observed experimental positions (Eq. S5 [43]). Finally, the parameters were further refined over 14 identified oxide reflections. The solution ($\chi^2 = 1.2$; Table III) is $a_{ox} = 18.8 \pm 0.2$ Å; $b_{ox} = 10.68 \pm 0.08$ Å; $\gamma_{ox} = 91.2 \pm 0.8°$; $\alpha_{ox} = 27.5 \pm 0.4°$. As shown in Table III, the unit cell of the oxide layer determined herein on oxidized $Fe_{0.85}Al_{0.15}(110)$ is seen to fairly compare to previous determinations on oxidized NiAl(110) [18,26,29], on oxidized FeAl(110) [91] and on aluminum oxide grown on a Ni(111) surface [89].

It is now possible to reconsider the LEED pattern analysis. The simulated LEED pattern based on the unit cell determined by GIXD agrees well with the experimental pattern [Fig. 6(c)], apart from the above-mentioned distortions and some spots that don't remain fully explained. Looking now at the main surface directions, the oxide structure is nearly commensurate with the substrate along $[10]_S = [1\bar{1}0]_B$ but incommensurate along the perpendicular one $[01]_S = [001]_B$ [Fig. 6(d)]. Compared to NiAl(110) or FeAl(110) (B_2/CsCl structure), the random alloy $Fe_{0.85}Al_{0.15}$ (A_2/bcc structure) offers in terms of symmetry an extra degree of coincidence due to the centering of the surface unit cell. In Fig. 6(d), the comparison with the
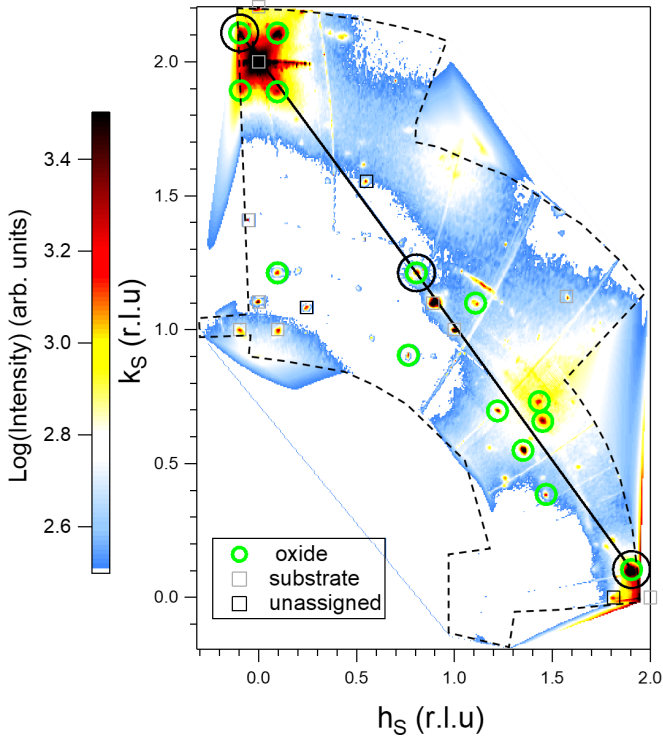
FIG. 8. In-plane diffraction map ($l_S = 0.075$) of the oxidized Fe$_{0.85}$Al$_{0.15}$(110) surface. The scanned part of reciprocal space is surrounded by a dotted line; the color outside is an artifact of data interpolation. The main peaks are highlighted, in particular those that stem from diffraction of the oxide layer (green spots); the perfectly aligned spots (green circled in black) were used for unit cell indexing (see text). Raw data are shown in Fig. S5 [43].

substrate primitive unit cells (grey grid) shows that the oxide cell is in coincidence along $2\mathbf{b}_{ox}$ (within 0.2%) and nearly along $\mathbf{a}_{ox}$ (within 2%). Calculations show that this coincidence of the (1×2) oxide supercell is within the error bars of the

GIXD determination. Finally, diffraction results indicate that the antiphase domain boundaries seen in STM [Figs. 2(a) and 2(c)], that appear every 8–12 nm, run along the diagonal of the oxide unit cell or along $\mathbf{b}_{ox}$, exactly like on NiAl(110) [18,26,45,46,72–76], probably to release the strain due to the misfit with the substrate.

VI. *AB INITIO* SIMULATIONS OF CORE-LEVEL SHIFTS

To further explore the case, atomistic simulations were performed to test if the unique existing model of alumina/NiAl could also account for the electronic characteristics of the present oxide film. To this goal, the alumina film (Fig. 9) proposed for NiAl(110) [29] was positioned on top of B2-CsCl FeAl(110), whose composition matches well the near-surface Fe/Al ratio found experimentally (Sec. IV B). While the film and substrate atomic structures were thoroughly relaxed, the hypothesis of an ordered alloy surface was maintained and a (1×2) commensurate oxide unit cell was used, in agreement with the observed similarity of lattice parameters (Sec. V). A comparison between calculated CLSs with the measured values is shown in Table IV. The overall agreement is quite satisfactory, in particular regarding (i) the shift between the weakly and strongly bound O $1s$ levels and (ii) the CLS of the Al atoms in the interfacial and surface layers with respect to Al in bulk FeAl. The calculations indicate that the substrate Al atoms at the interface display an average CLS of $+0.3$ eV with respect to the bulk; this shift is hidden experimentally in the resolution and the gradient of Al concentration between the surface and the bulk. An additional agreement is found between the relative areas of the two components of Al $2p$ and O $1s$ core levels (Tables I and II) and the theoretical number of involved atoms (Table IV). At normal emission where signal damping is expected to be of minor importance for the bilayer structure, the experimental ratio is 0.23 (respectively, 1.6) for O $1s$ (respectively, Al $2p$) core levels compared to 0.18 (respectively, 1.5) for the number of involved atoms in the

TABLE III. Aluminum oxide unit cell parameters at the surface of metallic substrates as determined in the literature. The substrate (bulk lattice parameter a_B) is designated by its Strukturbericht symbol [54] and parent compound. M_S corresponds to the superstructure matrix from the substrate rectangular surface unit cell. Other quantities are defined in Fig. 6(d).

| Work	Substrate	a_B, (a_S, b_S) (Å)	a_{ox} (Å)	b_{ox} (Å)	γ_{ox}(deg)	α_{ox} (deg)	M_S	
SPA-LEED [26]	NiAl(110)	2.887	17.89	10.55	88.67	24.1	$\begin{bmatrix} 4 & 2.53 \\ -1 & 3.37 \end{bmatrix}$	
	B$_2$-CsCl	4.083×2.887						
GIXD [18]	NiAl(110)	2.887	18.01	10.59	91.15	24.01	$\begin{bmatrix} 4.03 & 2.54 \\ -1.10 & 3.32 \end{bmatrix}$	
	B$_2$-CsCl	4.083×2.887						
DFT [29]	NiAl(110)	2.895	17.9	10.93	91.84	–	–	
	B$_2$-CsCl	4.094×2.895						
GIXD [89]	Al/Ni(111)	3.524	18.23	10.53	90	–	–	
	A$_1$-fcc	2.491×2.491						
LEED [91]	FeAl(110)	2.906	18.01	10.62	88.66	24.1	$\begin{bmatrix} 4. & 2.53 \\ -1 & 3.37 \end{bmatrix}$	
	B$_2$-CsCl	4.110×2.9064						
GIXD	Fe$_{0.85}$Al$_{0.15}$(110)	2.888	18.8	10.68	91.2	27.5	$\begin{bmatrix} 4.08 & 3.01 \\ -1.25 & 3.24 \end{bmatrix}$	
This paper	A$_2$-bcc	4.091×2.888	± 0.2	± 0.08	± 0.8	± 0.4		
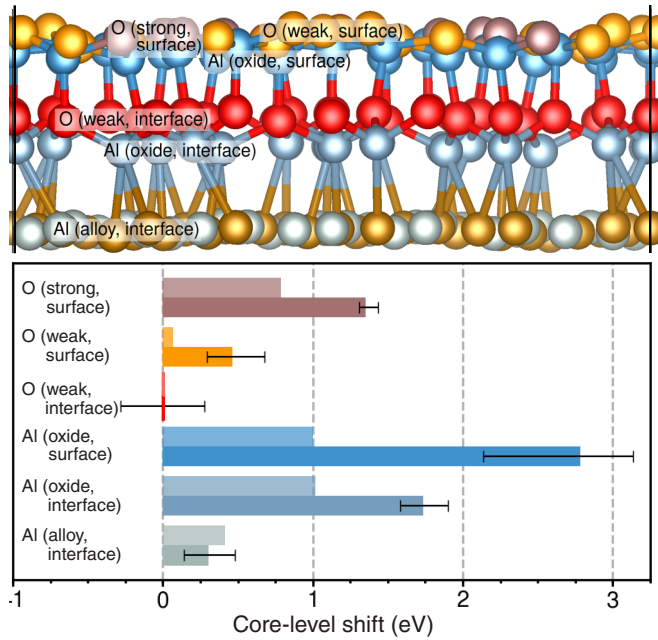
FIG. 9. Top panel: Side view of the supported oxide layer on FeAl(110). Bottom panel: Averaged Al $2p$ and O $1s$ CLS for the different atom types in the complete screening and the initial state pictures (darker and lighter colors, respectively). The bars indicate the corresponding minimal and maximal values. The Al $2p$ and O $1s$ references are the bulklike Al in the middle of the FeAl substrate layer and the average binding energy of the interfacial O atoms, respectively.

present model. Very close values have also been determined for the oxide at NiAl(110) surface (0.19/1.5) [31]. The switch from normal to grazing emission leads to a systematic enhancement of the high-/low-binding energy area ratio in close agreement with the expected exponential damping of signal with inelastic mean-free path given in Table SI [43] and the half-film thickness (bilayer) determined in Sec. IV C. This is in line with minor effects of photodiffraction at AlK-α energies as suggested by Ref. [31]. Finally, the larger Gaussian broadening of the oxide components compared to the metallic one (Tables I and II) reflects the calculated distribution of CLSs.

To reach a more detailed understanding of the origin of the different O $1s$ and Al $2p$ components, the initial state and complete screening CLS are furthermore shown in Fig. 9. Three types of O atoms can be distinguished based on their O $1s$ level. Comparatively weak binding energies are found for O core levels in the interfacial layer (red), as well as for most O core levels at the oxide surface (orange). Note that in Table IV, as in Ref. [31], these first two types have been grouped into one component. The third kind, at significantly higher binding energies, corresponds to 28% of the O atoms at the surface (purple). In Ref. [31], this shift to higher binding energies has been ascribed to the presence of an interfacial Al atom below the surface O atoms in question, combined with a comparatively low number of other surface O atoms in the immediate vicinity. This interpretation in terms of shifts in the local electrostatic potential is supported by the calculated initial state contribution shown in Fig. 9. For both kinds of surface oxygen atoms (orange and purple), however, final state effects are also significant. This is consistent with less efficient screening of the core hole at the surface layers compared to the interface, which can in turn be connected to the increased distance to the metallic substrate. A similar combination of initial and final state contributions lies at the origin of the Al $2p$ CLS. Compared to the Al atoms in the bulk and surface of the FeAl substrate, the Al core levels in the oxide adlayer (blue gray and light blue) display more positive binding energies due to initial state effects associated with an increase in oxidation state. The total shifts are then enhanced by final state contributions, with different amounts for the Al atoms in the interfacial layer and at the oxide surface, similar to the O $1s$ case.

The CLS values found herein on FeAl(110) are close to those observed on oxidized NiAl(110) [29,31], and a similar level of agreement is obtained between measurements and calculations for the two systems (see Table IV). The most noticeable structural difference consists of only a small (0.7%) isotropic compression which is due to the reduction in lattice constant from NiAl (2.879 Å) to FeAl (2.859 Å) and the assumed unit-cell matching. However, regarding the electronic characteristics, FeAl is found somewhat more ionic (4% larger Bader charges) and its calculated surface work function somewhat (4%) smaller. Therefore, the tendency toward larger Al $2p$ shifts for Al atoms in the oxide on FeAl does not result

TABLE IV. Comparison of the experimental and calculated core-level shifts (CLSs) for the ultrathin oxide layer on NiAl(110) and FeAl(110). The positions of the different atom types are indicated in Fig. 9.

	FeAl(110)		NiAl(110)			
Component	Expt. (Present paper)	Calc. (Present paper)	Expt. Ref. [31]	Calc. Ref. [31]	Calc. (Present paper)	Number of atoms
Al (alloy, bulk)	0.00	0.00	0.00	0.00	0.00	–
Al (alloy, interface)	–	$+0.14 \rightarrow +0.48$	-0.10	$-0.60 \rightarrow -0.30$	$-0.25 \rightarrow +0.06$	17
Al (oxide, interface)	$+1.80$	$+1.58 \rightarrow +1.90$	$+1.00$	$+1.00 \rightarrow +1.40$	$+1.06 \rightarrow +1.34$	16
Al (oxide, surface)	$+2.9$	$+2.14 \rightarrow +3.13$	$+2.27$	$+1.71 \rightarrow +2.67$	$+1.61 \rightarrow +2.65$	24
O (weak)	0.00	$-0.46 \rightarrow +0.50$	0.00	$-0.41 \rightarrow +0.54$	$-0.47 \rightarrow +0.46$	44
O (strong)	$+1.17$	$+1.13 \rightarrow +1.25$	$+1.23$	$+1.05 \rightarrow +1.14$	$+1.15 \rightarrow +1.26$	8
M (alloy, bulk)	–	0.00	–	–	0.00	–
M (alloy, interface)	–	$-0.14 \rightarrow +0.37$	–	–	$-0.37 \rightarrow +0.32$	17

from structural or chemical changes in the adlayer, but rather from the different bulk references for the Al core level.

VII. DISCUSSION AND CONCLUSION

All the above-presented clues point to an oxide structure on Fe$_{0.85}$Al$_{0.15}$(110) similar to that found on NiAl(110) [29], in spite of a growth on a random alloy having the freedom to segregate. As seen from photoemission, the subsurface below the oxide keeps a composition close to a B$_2$ structure (Fe$_{0.6}$Al$_{0.4}$) over a typical depth of 3 nm, as on the metallic surface. Nevertheless, the complex reconstruction observed on the bare surface [54] is partly lifted by the oxidation process. In the same way as on NiAl(110), the film thickness is self-limited to a ~7.5 Å thick bilayer. Diffraction shows that the oxide layer displays two domains having a nearly rectangular unit cell very close to that determined in the only two accurate analyses (NiAl(110) [18,26] and Al/Ni(111) [89]; see Table III). The determined stoichiometry Al$_2$O$_{2.5\pm0.2}$ is similar to that found on NiAl(110) (Al$_{10}$O$_{13}$) [29]. As on this substrate, dense antiphase domain boundaries (8–12 nm width) have been evidenced by STM. At last, according to *ab initio* simulations, the Al 2p and O 1s CLSs and relative intensities are identical to those found for the oxide on NiAl(110) within differences that stand mainly for different Al core-level bulk references.

Modulo a few distorsions, the oxide structure determined on NiAl(110) [29] seems to be stable on supports of different symmetries and compositions. Beyond NiAl(110) and Al/Ni(111), the observed oxide LEED pattern shares some similarities with those obtained on Fe$_{0.47}$Al$_{0.53}$(110) [9], Cu-9 at. %Al(111) [15] and the complex alloy γ-Al$_4$Cu$_9$(110) [92]. The actual role of the substrate in its formation is still puzzling. Prévot *et al.* argued that it is an archetype of free-standing oxide [89] since, according to their diffraction study, the presence of the oxide poorly affects the atomic positions of Ni(111). As an extension of this idea, the astonishing similarity between the present FeAl case and NiAl suggests that, if the aluminum oxidizes independently of the surface, the close crystallography of the substrate unit cells leads to iron anchors distributed in a comparable geometry. Indeed, in agreement with NiAl(110), alumina layer on Fe$_{0.85}$Al$_{0.15}$(110) is strained due to mismatch with the substrate leading to dense antiphase boundaries.

The ubiquity of the ultrathin oxide structure grown at the surface of various metallic substrates asks for the reason of its peculiar stability and the mechanism of structural transition toward thicker bulklike alumina films obtained at higher oxygen activities.

[1] M. Finnis, A. Lozovoi, and A. Alavi, Surf. Sci. **35**, 167 (2005).

[2] Q. Wu, A. Fortunelli, and G. Granozzi, Int. Rev. Phys. Chem. **28**, 517 (2009).

[3] S. Swaminathan and M. Spiegel, Appl. Surf. Sci. **253**, 4607 (2007).

[4] J. Zimmermann and L. Colombi Ciacchi, J. Phys. Chem. Lett. **1**, 2343 (2010).

[5] B. Demczyk, J. Vac. Sci. Technol. A **11**, 1458 (1993).

[6] G. Wood, Oxid. Met. **2**, 11 (1970).

[7] L. Latu-Romain, S. Mathieu, M. Vilasi, G. Renou, S. Coindeau, A. Galerie, and Y. Wouters, Oxid. Met. **88**, 481 (2017).

[8] H. Grabke, Intermetallics **7**, 1153 (1999).

[9] H. Graupner, L. Hammer, K. Heinz, and D. Zehner, Surf. Sci. **380**, 335 (1997).

[10] O. Kizilkaya, D. Hite, D. Zehner, and P. Sprunger, Surf. Sci. **529**, 223 (2003).

[11] O. Kizilkaya, I. Senevirathne, and P. Sprunger, J. Appl. Phys. **101**, 063706 (2007).

[12] C. Xu, W. Gao, and Y. He, Scr. Mater. **42**, 975 (2000).

[13] M. Yoshitake, S. Bera, and Y. Yamauchi, Surf. Interface Anal. **35**, 824 (2003).

[14] M. Yoshitake, W. Song, J. Libra, K. Mašek, F. Šutara, V. Matolín, and K. Prince, J. Appl. Phys. **103**, 033707 (2008).

[15] E. Napetschnig, M. Schmid, and P. Varga, Surf. Sci. **602**, 1750 (2008).

[16] V. Rose, V. Podgursky, I. Costina, R. Franchy, and H. Ibach, Surf. Sci. **577**, 139 (2005).

[17] V. Rose, V. Podgursky, I. Costina, and R. Franchy, Surf. Sci. **541**, 128 (2003).

[18] A. Stierle, F. Renner, R. Streitel, H. Dosch, W. Drube, and B. Cowie, Science **303**, 1652 (2004).

[19] S. Ulrich, N. Nilius, and H.-J. Freund, Surf. Sci. **601**, 4603 (2007).

[20] R. Franchy, J. Mausch, and P. Gassmann, Appl. Surf. Sci. **93**, 317 (1996).

[21] N. Cai, H. Qin, X. Tong, and G. Zhou, Surf. Sci. **618**, 20 (2013).

[22] G. Hamm, C. Barth, C. Becker, K. Wandelt, and C. R. Henry, Phys. Rev. Lett. **97**, 126106 (2006).

[23] O. Kurnosikov, L. Jurczyszyn, B. Pieczyrak, and A. Krupski, Surf. Sci. **602**, 2994 (2008).

[24] A. Rosenhahn, J. Schneider, C. Becker, and K. Wandelt, Appl. Surf. Sci. **142**, 169 (1999).

[25] R. M. Jaeger, H. Kuhlenbeck, H.-J. Freund, M. Wuttig, W. Hoffmann, R. Franchy, and H. Ibach, Surf. Sci. **259**, 235 (1991).

[26] J. Libuda, F. Winkelmann, M. Baumer, H. J. Freund, T. Bertrams, H. Neddermeyer, and K. Mailer, Surf. Sci. **318**, 61 (1994).

[27] A. Lozovoi, A. Alavi, and M. Finnis, Comput. Phys. Commun. **137**, 174 (2001).

[28] A. Stierle, C. Tieg, H. Dosch, V. Formoso, E. Lundgren, J. Andersen, L. Köhler, and G. Kresse, Surf. Sci. **529**, L263 (2003).

[29] G. Kresse, M. Schmid, E. Napetschnig, M. Shishkin, L. Köhler, and P. Varga, Science **308**, 1440 (2005).

[30] T. Lay, M. Yoshitake, and W. Song, Appl. Surf. Sci. **239**, 451 (2005).

[31] N. M. Martin, J. Knudsen, S. Blomberg, J. Gustafson, J. N. Andersen, E. Lundgren, H. H. Ingelsten, P.-A. Carlsson, M. Skoglundh, A. Stierle, and G. Kresse, Phys. Rev. B **83**, 125417 (2011).

[32] S. Deevi and V. Sikka, Intermetallics **4**, 357 (1996).

[33] W. Song and M. Yoshitake, Thin Solid Films **464**, 52 (2004).

[34] M. Yoshitake, T. Lay, and W. Song, Surf. Sci. **564**, 211 (2004).

[35] R. Franchy, Surf. Sci. Rep. **38**, 195 (2000).

[36] A. Stierle, V. Formoso, F. Comin, and R. Franchy, Surf. Sci. **467**, 85 (2000).

[37] D. Sondericker, F. Jona, and P. M. Marcus, Phys. Rev. B **34**, 6770 (1986).

[38] C. Wang and C.-Y. Wang, Surf. Sci. **602**, 2604 (2008).

[39] M. Bäumer and H.-J. Freund, Prog. Surf. Sci. **61**, 127 (1999).

[40] H. J. Freund and G. Pacchioni, Chem. Soc. Rev. **37**, 2224 (2008).

[41] M. Klimenkov, S. Nepijko, H. Kuhlenbeck, and H.-J. Freund, Surf. Sci. **385**, 66 (1997).

[42] G. Ceballos, Z. Song, J. Pascual, H.-P. Rust, H. Conrad, M. Bäumer, and H.-J. Freund, Chem. Phys. Lett. **359**, 41 (2002).

[43] See Supplemental Material at https://link.aps.org/supplemental/10.1103/PhysRevMaterials.4.074409 for complementary figures, equations, and tables about XPS and LEED analysis.

[44] G. H. Simon, T. König, M. Nilius, H.-P. Rust, M. Heyde, and H.-J. Freund, Phys. Rev. B **78**, 113401 (2008).

[45] G. Simon, T. König, H.-P. Rust, M. Heyde, and H.-J. Freund, New J. Phys. **11**, 093009 (2009).

[46] L. Heinke, L. Lichtenstein, G. H. Simon, T. König, M. Heyde, and H.-J. Freund, Phys. Rev. B **82**, 075430 (2010).

[47] Y. Li, J. Brndiar, Y. Naitoh, Y. Sugawara, and I. Štich, Nanotechnology **26**, 505704 (2015).

[48] Z. Dai, P. Borghetti, Y. Mouchaal, S. Chenot, P. David, J. Jupille, G. Cabailh, and R. Lazzari, Appl. Surf. Sci. **444**, 457 (2018).

[49] D. R. Jennison, C. Verdozzi, P. A. Schultz, and M. P. Sears, Phys. Rev. B **59**, R15605 (1999).

[50] D. Jennison and A. Bogicevic, Surf. Sci. **464**, 108 (2000).

[51] V. Vonk, C. Ellinger, N. Khorshidi, A. Vlad, A. Stierle, and H. Dosch, Phys. Rev. B **78**, 165426 (2008).

[52] R. Cavallotti, H.-L. Thi Le, J. Goniakowski, R. Lazzari, J. Jupille, A. Koltsov, and D. Loison, Phys. Chem. Chem. Phys. **18**, 3032 (2016).

[53] H.-L. Thi Le, R. Lazzari, J. Goniakowski, S. Cavallotti, R. Chenot, C. Noguera, J. Jupille, A. Koltsov, and J.-M. Mataigne, J. Phys. Chem. C **121**, 11464 (2017).

[54] Z. Dai, P. Borghetti, S. Chenot, P. David, J. Jupille, G. Cabailh, J. Goniakowski, and R. Lazzari, Appl. Surf. Sci. **492**, 886 (2019).

[55] Z. Dai, N. Alyabyeva, P. Borghetti, S. Chenot, P. David, A. Koltsov, G. Renaud, J. Jupille, G. Cabailh, and R. Lazzari, Appl. Surf. Sci. **509**, 145312 (2020).

[56] I. Horcas, R. Fernández, J. M. Gómez-Rodríguez, J. Colchero, J. Gómez-Herrero, and A. M. Baro, Rev. Sci. Instrum. **78**, 013705 (2007).

[57] M. Ellner and I. Park, Metall. Mater. Trans. A **33**, 3591 (2002).

[58] P. Hohenberg and W. Kohn, Phys. Rev. **136**, B864 (1964).

[59] W. Kohn and L. J. Sham, Phys. Rev. **140**, A1133 (1965).

[60] P. E. Blöchl, Phys. Rev. B **50**, 17953 (1994).

[61] G. Kresse and J. Hafner, Phys. Rev. B **49**, 14251 (1994).

[62] G. Kresse and J. Furthmüller, Phys. Rev. B **54**, 11169 (1996).

[63] G. Kresse and J. Furthmüller, Comp. Mater. Sci. **6**, 15 (1996).

[64] G. Kresse and D. Joubert, Phys. Rev. B **59**, 1758 (1999).

[65] J. Klimeš, D. R. Bowler, and A. Michaelides, J. Phys.: Condens. Matter **22**, 022201 (2010).

[66] J. Klimes, D. R. Bowler, and A. Michaelides, Phys. Rev. B **83**, 195131 (2011).

[67] A. D. Becke, J. Chem. Phys. **85**, 7184 (1986).

[68] M. Dion, H. Rydberg, E. Schroder, D. C. Langreth, and B. I. Lundqvist, Phys. Rev. Lett. **92**, 246401 (2004).

[69] M. Dion, H. Rydberg, E. Schröder, D. C. Langreth, and B. I. Lundqvist, Phys. Rev. Lett. **95**, 109902(E) (2005).

[70] L. Köhler and G. Kresse, Phys. Rev. B **70**, 165405 (2004).

[71] V. Nilsson, M. Van den Bossche, A. Hellman, and H. Grönbeck, Surf. Sci. **640**, 59 (2015).

[72] M. Kulawik, N. Nilius, H.-P. Rust, and H.-J. Freund, Phys. Rev. Lett. **91**, 256101 (2003).

[73] K. McCarty, J. Pierce, and C. Carter, Appl. Phys. Lett. **88**, 141902 (2006).

[74] M. Schmid, M. Shishkin, G. Kresse, E. Napetschnig, P. Varga, M. Kulawik, N. Nilius, H.-P. Rust, and H.-J. Freund, Phys. Rev. Lett. **97**, 046101 (2006).

[75] G. Simon, T. König, L. Heinke, L. Lichtenstein, M. Heyde, and H.-J. Freund, New J. Phys. **13**, 123028 (2011).

[76] K. Hojrup Hansen, T. Worren, S. Stempel, E. Lægsgaard, M. Bäumer, H.-J. Freund, F. Besenbacher, and I. Stensgaard, Phys. Rev. Lett. **83**, 4120 (1999).

[77] N. Nilius, M. Kulawik, H.-P. Rust, and H.-J. Freund, Phys. Rev. B **69**, 121401(R) (2004).

[78] J. F. Moulder, W. F. Stickle, P. E. Sobol, and K. D. Bomben, *Handbook of X-ray Photoelectron Spectroscopy*, edited by J. Chastian and R. C. J. King (Physical Electronics, Inc., Eden Prairie, Minnesota, 1995).

[79] C. D. Wagner, W. M. Riggs, L. E. Davis, J. F. Moulder, and G. E. Muilenberg, *Handbook of X-Ray Photoelectron spectroscopy* (Perkin-Elmer, Eden Prairie, 1979).

[80] NIST X-ray photoelectron spectroscopy database, https://srdata.nist.gov/xps/Default.aspx.

[81] http://www.webelements.com.

[82] D. Shirley, Phys. Rev. B **5**, 4709 (1972).

[83] S. Doniach and M. Sunjic, J. Phys. C: Solid State Phys. **3**, 285 (1970).

[84] N. Gleason and D. Strongin, Surf. Sci. **295**, 306 (1993).

[85] B. Predel, in *Ac-Ag... Au-Zr: Supplement to Subvolume IV/5A*, Landolt-Börnstein-Group IV Physical Chemistry 12A: Physical Chemistry (Springer-Verlag, Berlin, 2006), pp. 1–2.

[86] O. Kubaschewski, *Iron Binary Phase Diagrams* (Springer, Berlin, Heidelberg, 1982).

[87] V. Blum, On the interplay of surface segregation and bulk order in binary alloys: Structural investigations of iron and cobalt aluminium-based intermetallics, Ph.D. thesis, Erlangen-Nuremberg University, 2001.

[88] Z. Liu and Y. Chang, Metall. Mater. Trans. A **30**, 1081 (1999).

[89] G. Prévot, S. Le Moal, R. Bernard, B. Croset, R. Lazzari, and D. Schmaus, Phys. Rev. B **85**, 205450 (2012).

[90] LEEDpat, Version 4.2, utility by K.E. Hermann (FHI) and M.A. Van Hove (HKBU), Berlin / Hong Kong, 2014; see also http://www.fhi-berlin.mpg.de/KHsoftware/LEEDpat/index.html.

[91] H. Graupner, L. Hammer, K. Müller, and D. Zehner, Surf. Sci. **322**, 103 (1995).

[92] M. Wardé, J. Ledieu, L. Serkovic Loli, M. Herinx, M.-C. de Weerd, V. Fournée, S. Le Moal, and M.-G. Barthés-Labrousse, J. Phys.: Condens. Matter **26**, 485009 (2014).